The Astrophysical Journal, 1001:5 (12pp), 2026 April 10 https://doi.org/10.3847/1538-4357/ae5059

CubeSats Reach the Millisecond X-Ray Domain: Crab Pulsar Timing with SpIRIT/HERMES

Wladimiro Leone[1,2,3], R. Mearns[4], T. di Salvo[2], L. Burderi[5,6], M. Thomas[4], M. Trenti[4], F. Fiore[3], E. J. Marchesini[7], R. Campana[7,8], G. Baroni[3], M. Dafčíková[3,9], A. Anitra[2], Y. Evangelista[10], A. Sanna[5], S. Puccetti[11], R. Iaria[2], S. Barraclough[4], M. Ortiz del Castillo[4], R. Bertacin[11], P. Bellutti[12,13], G. Bertuccio[14,15], A. Chapman[16], G. Cabras[5], F. Ceraudo[10], T. Chen[17], M. Citossi[3], R. Crupi[18], G. Della Casa[10], E. Demenev[13], G. Dilillo[11,19], M. Feroci[10], F. Ficorella[13], M. Fiorini[20], N. Gao[17], A. Guzman[21], P. Hedderman[21], A. Hudrap[22], C. Labanti[7], G. La Rosa[6], P. Malcovati[23], J. McRobbie[4], F. Mele[10,14,15], G. Molera Calvés[24], J. Morgan[4], G. Morgante[7], B. Negri[11], D. Novel[13], P. Nogara[6], A. Nuti[10], E. O'Brien[4], G. Pepponi[13], M. Perri[25], A. Picciotto[13], R. Piazzolla[11], S. Pirrotta[11], S. Pliego Caballero[21], A. Rachevski[26], I. Rashevskaya[26], A. Riggio[5], F. Russo[6], A. Santangelo[21], G. Sottile[6], C. Tenzer[21], Y. Tao[4], S. Trevisan[1], A. Vacchi[18], G. Zampa[26], N. Zampa[18,26], S. Xiong[17], S. Yi[17], A. Woods[4], S. Zhang[17], and N. Zorzi[13]

[1] Department of Physics,University of Trento, Via Sommarive, 14, 38123, Povo, Italy
[2] Dipartimento di Fisica e Chimica "E. Segrè," University of Palermo, Via Archirafi subcampus., Via Archirafi, 36, 90123 Palermo, Italy
[3] INAF/Osservatorio Astronomico di Trieste, via G. Tiepolo 11, 34124 Trieste, Italy
[4] School of Physics, The University of Melbourne, Parkville, VIC 3010, Australia
[5] Dipartimento di Fisica, Università degli Studi di Cagliari, SP Monserrato-Sestu, km 0.7, 09042 Monserrato, Italy
[6] INAF/IASF Palermo, via Ugo La Malfa 153, 90146 Palermo, Italy
[7] INAF/OAS, Via Piero Gobetti, 93/3, 40129 Bologna, Italy
[8] INFN Sezione di Bologna, Viale Berti Pichat 6/2, 40127 Bologna, Italy
[9] Department of Theoretical Physics and Astrophysics, Masaryk University, Kotlárská 267/2, 611 37 Brno, Czechia
[10] INAF/IAPS, Via del Fosso del Cavaliere, 100, 00133 Roma, Italy
[11] ASI—Italian Space Agency, Via del Politecnico snc, 00133 Rome, Italy
[12] INAF/OAB, via E. Bianchi 46I-23807 Merate, Italy
[13] Fondazione Bruno Kessler—Sensors and Devices, Via Sommarive, 18, 38123 Povo, Italy
[14] Dept. Electronics, Information and Bioengineering, Politecnico di Milano, Via Giuseppe Ponzio, 34, 20133 Milano, Italy
[15] INFN Milano, Via Giovanni Celoria, 16, 20133 Milan, Italy
[16] Department of Mechanical Engineering, University of Melbourne, Parkville, VIC 3010, Australia
[17] IHEP/CAS, 19B Yuquan Road, Shijingshan District, Beijing, 100049, People's Republic of China
[18] Department of Mathematics, Computer Science and Physics, University of Udine, via delle Scienze, 206, 33100 Udine, Italy
[19] INAF, Osservatorio Astronomico di Roma, Via Frascati 33, Monte Porzio Catone, Roma 00040, Italy
[20] INAF/IASF Milano, Via Alfonso Corti 12, 20133 Milano, Italy
[21] Institut für Astronomie und Astrophysik, Sand 1, 72076, Tübingen, Germany
[22] Skylabs, Zagrebška c. 104, 2000 Maribor, Slovenia
[23] Dipartimento di Ingegneria Industriale e dell'Informazione, University of Pavia, Via Adolfo Ferrata 5, 27100 Pavia, Italy
[24] Department of Physics, University of Tasmania, Clark Road, Hobart, TAS 7005, Australia
[25] INAF/OAR, Via Frascati 33, 00040 Monte Porzio Catone, Italy
[26] INFN Trieste, Padriciano, 99, 34149 Trieste, Italy

Received 2026 January 19; revised 2026 March 5; accepted 2026 March 9; published 2026 April 1

Abstract

The High Energy Rapid Modular Ensemble of Satellites (HERMES) instrument is a compact X-/gamma-ray spectrometer operating on board the 6U (11 kg) Space Industry–Responsive–Intelligent–Thermal (SpIRIT) CubeSat. The payload is particularly well suited for the observation of cosmic transients such as gamma-ray bursts (GRBs) and bright pulsars thanks to its unique broadband sensitivity from a few keV to a few MeV and temporal resolution down to half a microsecond. We report the detection of the ∼33 ms double-peaked pulse profile of the Crab Pulsar, obtained by considering the canonical Crab ephemerides as provided by the Jodrell Bank catalog. We collected approximately 5.7×10^4 photons from 730 s of observations in the 3 keV–2 MeV energy band during a single operation, achieving a 5σ pulse-profile significance in the 3–11.5 keV energy band with millisecond-scale binning. These results demonstrate that SpIRIT/HERMES can achieve millisecond timing accuracy at high energies and, thanks to its wide field of view and broad energy coverage, has the potential to contribute to GRB monitoring in the near future. Such capabilities were previously the domain of flagship observatories, underscoring the performance of the HERMES instrument even with its compact form factor.

Unified Astronomy Thesaurus concepts: High energy astrophysics (739); Pulsar timing method (1305); Spectrometers (1554)

1. Introduction

High-energy astrophysics in the X-ray and gamma-ray bands has traditionally been driven by large spaceborne observatories, whose substantial collecting area, stable pointing, and precise timing have enabled detailed studies of

compact objects and fast variability. Missions such as the Rossi X-ray Timing Explorer (RXTE), the Nuclear Spectroscopic Telescope Array (NuSTAR), and the Neutron Star Interior Composition Explorer (NICER) have established the current state of the art in sensitivity and absolute timing, providing key insights into pulsars, accreting systems, and high-energy transients (J. H. Swank 1999; M. van der Klis 2006; K. K. Madsen et al. 2015; M. Vivekanand 2021). In recent years, advances in detector technology and onboard electronics have enabled CubeSat-class missions to access the X-ray and gamma-ray sky with compact detectors and increasing scientific maturity, particularly in the context of time-domain and transient astrophysics (A. Pál et al. 2023; T. Tamagawa et al. 2025).

The High Energy Rapid Modular Ensemble of Satellites (HERMES) payload is an innovative and compact ($\sim$1 U, i.e., $10 \times 10 \times 10\,\mathrm{cm}^3$ volume, with $\approx$1.6 kg mass) X/gamma-ray spectrometer operating in orbit on board the 6U Space Industry–Responsive–Intelligent–Thermal (SpIRIT) nanosatellite CubeSat (M. Trenti et al. 2024). The payload adopts, for the first time in space, a silicon sandwich (siswich) architecture, in which silicon drift detectors (SDDs) are used both to detect (i) cosmic X-rays directly and (ii) gamma rays via optical photons produced by scintillation in cerium-doped gadolinium-aluminum-gallium garnet (GAGG:Ce) crystals (Y. Evangelista et al. 2021, 2024). This provides unique broadband sensitivity from a few keV to a few MeV. A second key feature of the HERMES payload is its exquisite event timing. While the siswich configuration enables fast event-by-event readout, the submicrosecond performance is primarily set by the back-end time-tagging chain. The resulting time resolution is $\sim$0.5 μs, about 5–7 times better than that of previous instruments dedicated to this task (R. Campana et al. 2022; G. Dilillo et al. 2024).

The instrument has been developed as the core element of the HERMES (+SpIRIT) Pathfinder, an in-orbit demonstration mission consisting of a constellation of six 3U and one 6U CubeSats (F. Fiore et al. 2021, 2025), each equipped with an identical payload (Y. Evangelista et al. 2021). Pathfinder aims to detect and contribute to the localization of high-energy astrophysical transients, such as gamma-ray bursts (GRBs), with high timing precision, broad sky coverage, and good sensitivity. The detection threshold photon flux (at 1 s for long and 64 ms for short GRBs) in the 50–300 keV band is 0.8 ph $\mathrm{cm}^{-2}\,\mathrm{s}^{-1}$ for long GRBs and 5.6 ph $\mathrm{cm}^{-2}\,\mathrm{s}^{-1}$ for short GRBs (G. Ghirlanda et al. 2024). The mission architecture leverages a distributed, modular approach to improve responsiveness and localization accuracy through inter-satellite temporal triangulation techniques (K. Hurley et al. 2013; F. Fiore et al. 2021; M. Thomas et al. 2023; W. Leone et al. 2025).

This paper presents the first timing analysis of Crab Pulsar data obtained with the HERMES payload on board SpIRIT. The Crab is a composite system consisting of a young pulsar (PSR B0531+21) and a surrounding synchrotron nebula, and is one of the most widely used calibration sources in high-energy astrophysics. Both the pulsar and the nebula emit across the entire electromagnetic spectrum. Because of its high and stable flux, especially in the X-ray and gamma-ray bands, the Crab is considered a "standard candle" for instrument verification (M. G. Kirsch et al. 2005). Furthermore, the Crab pulsation, characterized by a well-known double-peaked profile with a period of about 33 ms, is widely used to evaluate the timing accuracy of many instruments (A. H. Rots et al. 2004). In this work, we present the detection of the Crab Pulsar profile with HERMES. Independently, a similar result was recently obtained by another CubeSat mission, Ninjasat, using an X-ray gas detector sensitive in the 2–50 keV band (T. Tamagawa et al. 2025). This result was achieved with an exposure of 11 ks and a collimator that narrows the field of view (FOV) to $\approx 2\overset{\circ}{.}1$, thereby substantially reducing the nonpulsed contribution from the cosmic X-ray background. Both results demonstrate that a CubeSat-class, low-cost mission can deliver timing performance previously achievable only with larger, dedicated observatories, marking a step toward precision time-domain astrophysics from nanosatellites.

This paper is organized as follows. Section 2 summarizes the SpIRIT/HERMES characteristics and science operations. Section 3 presents the Crab Pulsar timing analysis and the pulse-profile determination using the SpIRIT/HERMES non-collimated detector with a total exposure of 730 s. Section 4 compares the timing capabilities of SpIRIT/HERMES with those of the NuSTAR and NICER observatories and validates the detected SpIRIT/HERMES pulse profile by modeling it against the NuSTAR profile.

Finally, the Appendix demonstrates both analytically and via Monte Carlo tests that the relatively short exposure time considered in this analysis is expected to lead to a significant Crab detection with SpIRIT/HERMES, as inferred from the observations.

2. SpIRIT/HERMES

The first HERMES payload was launched and operated in space thanks to international cooperation between Australia and Italy. In this section, we present an overview of the SpIRIT mission and of the early in-orbit operations of HERMES.

2.1. The SpIRIT Satellite

The SpIRIT satellite is a 6U-XL nanosatellite, launched into a Sun-synchronous orbit on 2023 December 1 (M. Trenti et al. 2024). At the time of writing, it has been successfully and continuously operating for over 2 yr in orbit. Elements funded by the Australian Space Agency include the spacecraft platform, supplied by an Australian commercial provider, an instrument control unit, i.e., the Payload Management System (PMS; M. O. del Castillo et al. 2025), a thermal control unit (TheMIS; M. Ortiz del Castillo et al. 2024a), an iridium and GPS payload (R. Mearns et al. 2024), and a graphic processing unit and multicamera system (M. Ortiz del Castillo et al. 2024b), all developed by the University of Melbourne. The HERMES payload and the *S*-band module were supplied by the Italian Space Agency through a cooperative agreement with the University of Melbourne.

2.2. The HERMES Payload

Each HERMES detector comprises 60 GAGG:Ce inorganic scintillator crystals (with a cross-sectional area of 6.94×12.1 mm^2 and a thickness of 15 mm) coupled to 12 arrays of 2×5 SDD cells (Y. Evangelista et al. 2021; R. Campana et al. 2022), each with a 25 mm^2 sensitive area, segmented into four independent quadrants of 30 SDD cells each. Thanks to their sensitivity to both X-ray and optical photons, SDDs provide a dual readout channel: They detect low-energy X-rays directly in the silicon (X-mode) and, when coupled to a scintillator,

they also detect gamma rays indirectly by collecting the optical scintillation light produced in the crystal (S-mode). In the baseline layout, each crystal is optically coupled to two SDD cells, so that the resulting light-sharing pattern enables a reliable discrimination between X- and S-events (R. Campana et al. 2024). This so-called "siswich" architecture offers wide spectral sensitivity, spanning a few keV to several MeV, and exceptional time resolution, reaching submicrosecond precision, thanks to the fast response of the GAGG:Ce crystals and the fine segmentation of the SDD mosaics (R. Campana et al. 2024). An onboard chip-scale atomic clock provides an extremely stable 10 MHz clock (which can be synchronized with the GPS pulse-per-second signal) for accurate time-tagging of the events (R. Campana et al. 2024). The SDD signals are read out by the application-specific integrated circuit (or ASIC), called LYRA (M. Gandola et al. 2021), a multichip architecture of 120 front-end chips (LYRA-FE), placed in close proximity to the SDD anodes, and four 32 channel back-end chips (LYRA-BE), using an innovative current-mode transmission strategy that minimizes interchannel crosstalk while maintaining low noise and low ($<1\,\mathrm{mW\,ch^{-1}}$) power consumption. The payload FOV is energy dependent: It is $\sim$3 sr in the 3–20 keV band and broadens at higher energies as the shielding becomes less effective, reaching $\sim$5 sr above 50 keV (R. Campana et al. 2021; G. Ghirlanda et al. 2024).

The payload on SpIRIT achieved first light in 2024 February. Since then, it has been operated as part of the satellite commissioning phase and for in-orbit calibration (G. Baroni et al. 2024). Unfortunately, prior to delivery of the payload to the University of Melbourne for integration, one of the four HERMES quadrants was damaged, and thus has not been operational since integration on the spacecraft. This results in an overall reduction of about 25% in effective area (with an associated sensitivity reduction of $\sqrt{0.75}$), which is accounted for in the analysis presented in this paper.

During Crab Pulsar observations, the nominal low-energy threshold for each active channel ranges from 3 to 7 keV, due to variations in the channel-to-channel process and the working principle of the discrimination circuit (Y. Evangelista et al. 2021). Accordingly, throughout this paper we adopt 3 keV as the minimum energy of the HERMES effective area to ensure that any potential source photons are included in the analysis.

2.3. SpIRIT Operations

As SpIRIT represents the first satellite launched by the University of Melbourne and by the commercial platform provider, as well as the first flight of the HERMES payload, a protracted commissioning period followed, with a number of operational limitations and anomalies accruing over the operating lifetime. These have had an impact on the execution and design of HERMES observational operations, and so are briefly outlined here.

1. The spacecraft platform provides a scripting engine to organize and schedule custom operations; however, these scripts are limited to a critical maximum memory size,[27] which introduces significant challenges in scheduling complex operations such as those associated with a scientific instrument.
2. The PMS instrument control unit provides an interface between all SpIRIT payloads, including the HERMES instrument, and the spacecraft platform, granting onboard data storage, power management, and a command-line interface via the platform scripting engine that allows flexible operations. The HERMES instrument is preferentially supplied with an uninterruptible power supply by the PMS to forestall any power supply issues (M. O. del Castillo et al. 2025). Unfortunately, following deployment of the second solar panel in 2024 July, the PMS has experienced randomly occurring resets at a rate of approximately 6 resets $\mathrm{hr^{-1}}$. While a direct root cause of these resets has not been identified to date, there appears to be a strong geographic correlation, which interestingly excludes regions of high radiation such as the South Atlantic Anomaly (M. Ortiz del Castillo et al. 2026, in preparation). These PMS anomalies have directly affected the operational cadence of the HERMES instrument, with early commissioning operations, such as this observation of the Crab Pulsar/Nebula, directly terminated by any single reset.
3. Since launch, SpIRIT has been affected by a number of limitations of the Attitude and Determination Control system (ADCS). Primarily, SpIRIT has a strong intrinsic magnetic dipole of the order of 0.6 A $\mathrm{m^2}$ (J. Wen et al. 2026, in preparation). When this field interacts with Earth's magnetic field, a significant torque can be induced on the spacecraft. Consequently, the spacecraft reaction wheels must rapidly increase speed to compensate. Once the safety threshold of the wheels is exceeded, the spacecraft must enter a "detumbling" period in which the wheels are slowed, the spacecraft tumbles, and the angular momentum is slowly bled out of the spacecraft using magnetorquers. Due to the strength of the intrinsic magnetic field, such detumbling periods can occur as frequently as every orbit if SpIRIT maintains a fixed attitude for an extended period. Critically, in order to achieve an acceptable level of attitude determination and control during eclipse, the SpIRIT star tracker must be pointed as close to zenith as possible. However, fixing both the HERMES instrument boresight and the star-tracker boresight (orthogonal vectors) for an extended period results in an attitude that is particularly susceptible to momentum buildup from the intrinsic dipole. This anomaly therefore further limits the possible operational cadence of the HERMES instrument during observations of a particular astrophysical source.
4. Due to both the ADCS and PMS anomalies, commissioning of the payload GPS timing source was not possible prior to this observation. Consequently, absolute timing information is provided to the payload by means of a "mock" GPS signal. This mock signal is synchronized to the platform's GPS clock with an uncertainty of up to 1 s (the mock signal synchronization is rounded down to the nearest second) and provided to the HERMES instrument once a second. Following a PMS reset, the HERMES payload goes through a safe shutdown sequence, during which its internal atomic clock is turned off. Therefore, high-precision photon arrival times are limited to a single uninterrupted

[27] The actual value is proprietary commercial information of the platform provider, and experience in orbit has shown variability depending on other processes running on board.

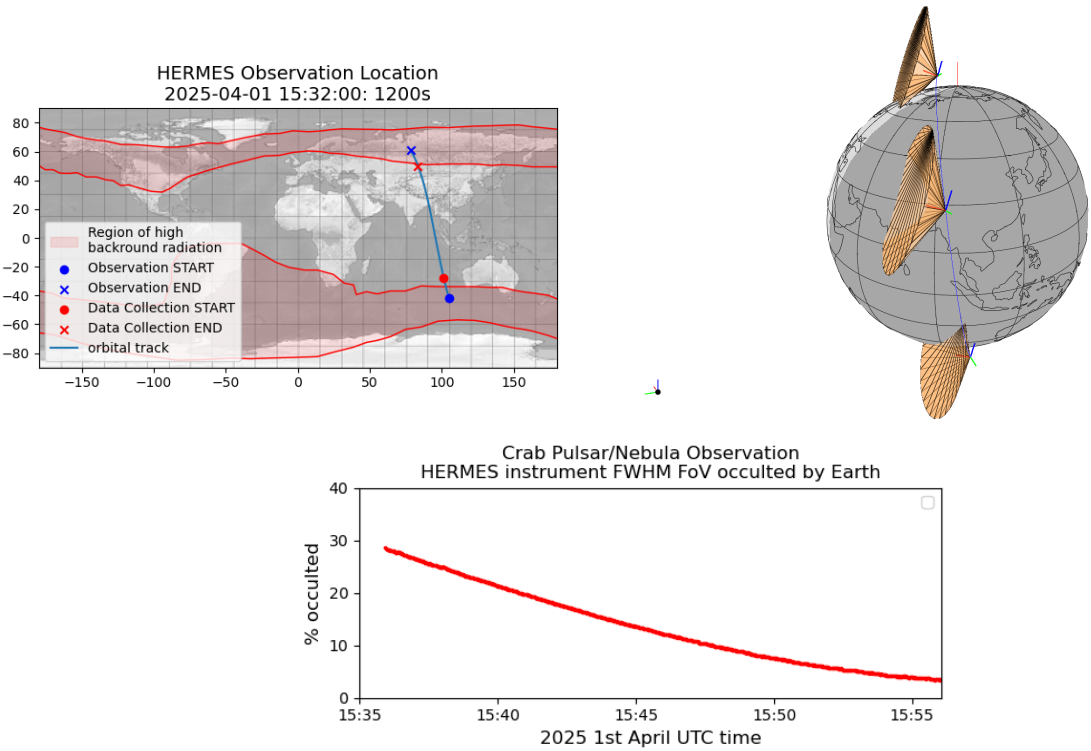

Figure 1. SpIRIT and HERMES instrument FOV configuration during the Crab Pulsar/Nebula observation. Top left: orbital track of SpIRIT during data collection, with high-background regions shown in shaded red; data collection began on 2025 April 1 at 15:36:06 UTC and ended on 2025 April 1 at 15:56:06 UTC. Top right: three-dimensional display of the SpIRIT location and HERMES instrument FOV during the operation. Bottom: HERMES FOV occultation by Earth during the observation (used for background noise estimation).

operation with HERMES (i.e., consistent tracking/phase connection between observing segments in time is not ensured across the power-cycling boundary).

5. SpIRIT carries an *S*-band radio for payload data downlink that was planned for use through the HERMES TP/SP ground segment. However, this link had not been commissioned at the time of these observations. Therefore, all payload data reported in this paper were downlinked via the Telemetry and TeleCommand link provided by the UHF radio. This limits the overall transmission rate of payload data to about 200 kB day^{-1}, after accounting for higher-priority spacecraft health telemetry. As a result, the planning, execution, data retrieval, and analysis iterative loop during commissioning activities was protracted. In fact, considering the time needed for uplink of telecommands, typically one iterative set of experiments could be done on a timescale of 1 week.
6. Due to risk aversion to avoid exposing the HERMES instrument to direct sunlight during operations in case of loss of attitude control, operations at the time of data acquisition were limited to eclipse periods.

We note that the presence of anomalies and in-orbit limitations relative to the preflight nominal configuration is typical for CubeSat missions, particularly for first flights. This is exemplified by the historical failure rate of CubeSats, with about 40% probability of infant mortality for university-led CubeSats ("dead on arrival" or loss of contact within 30 days postlaunch).[28] Therefore, by this metric, the successful operation for 2 yr of a complex multiorganization CubeSat such as SpIRIT, carrying both technology demonstration payloads and scientific instruments, represents a successful outcome—albeit with challenges.

2.4. HERMES Observations of the Crab Pulsar

Designing the observation of the Crab Pulsar with the SpIRIT nanosatellite is a complex, multiconstraint optimization problem. The instrument must be operated in regions of low background radiation between the radiation belts (the contours pictured in the top-left panel of Figure 1) and also simultaneously in eclipse. Further, the Crab Pulsar should be positioned as close to the spacecraft zenith (i.e., the center of the HERMES FOV) as possible during the observation to maximize the effective collecting area for photons. Competing with these constraints, however, are those to ensure the reliable operation of the platform throughout the observation. To minimize the chance of anomalous PMS resets, the observation should occur over geographic regions with a recorded low likelihood of resets (primarily above the Indian and Atlantic oceans). Additionally, to ensure a continuous attitude solution (and thereby ensure that the Crab Pulsar remains stable in the HERMES FOV), the SpIRIT star tracker must point as close to zenith as possible.

Given these constraints, the observational campaign of the Crab Pulsar/Nebula began in 2024 mid-December, with 25 observation attempts made over the following months to refine the process, mitigate errors within HERMES, the payload suite, and the platform, and obtain a sufficiently long dataset for the extraction of a pulsed signal. Figure 2 details the outcome of all observational attempts throughout this campaign. While only the primary failure mode of each

[28] https://digitalcommons.usu.edu/cgi/viewcontent.cgi?article=3415&context=smallsat

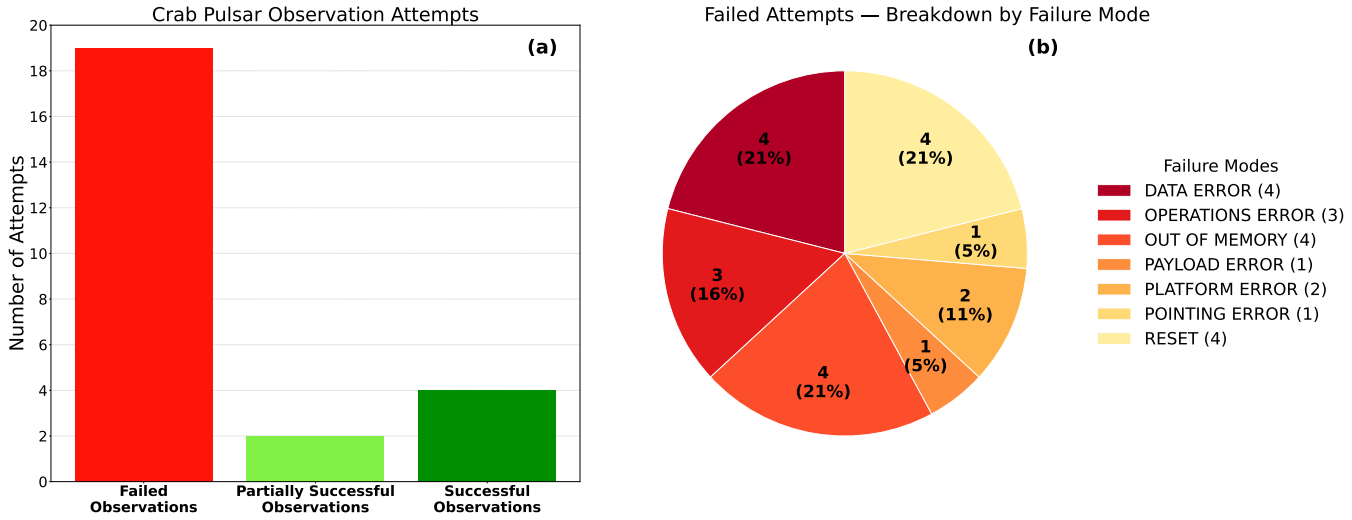

Figure 2. (a) Observation success statistics for the SpIRIT Crab Pulsar/Nebula observing campaign from 2024 December 11 to 2025 April 1. (b) Breakdown of the failed observation attempts by failure category.

observation attempt is listed, additional faults may have occurred. Of particular note as a secondary failure mode is insufficient attitude control for the duration of the observation. A brief description of each of the operation success status classifications follows.

1. *Observation attempt failure mode.*
   a. *DATA ERROR.* Due to a design limitation in the (early) version of the instrument flight software delivered for SpIRIT, more than 30% of data files above a size threshold could not be offloaded from the HERMES instrument.
   b. *OPERATIONS ERROR.* Resources were unavailable to the platform due to mission operations center errors.
   c. *OUT OF MEMORY.* The operational scripts for telecommanding the observation exceeded onboard memory limitations (this typically occurs as modifications to the operational script are rolled out to the spacecraft for the first time in order to mitigate other systematic problems).
   d. *PAYLOAD ERROR.* The HERMES instrument failed to respond to a request within the timeout period, terminating the observation.
   e. *PLATFORM ERROR.* The observation was not run due to onboard corruption of the schedule file or other recoverable platform software/hardware issues.
   f. *POINTING ERROR.* No other fault occurred, but the spacecraft ADCS could not maintain an attitude lock on the Crab Pulsar/Nebula sufficient to meet the scientific observation requirements.
   g. *RESET.* An anomalous PMS reset terminated the HERMES observation.
2. *Partially successful observations.* Similar to the aforementioned DATA ERROR classification, but in this case more than 70% of data files could be offloaded from the HERMES instrument.
3. *Successful observations.* No faults occurred during the operation, and a sufficient fraction of data files could be offloaded from the HERMES instrument.

Most failed observations were scheduled as single ∼40 s exposures. Successful detections of the Crab were obtained in three separate ∼40 s exposures and in longer integrations of ∼250 s, ∼400 s, and ∼700 s, the latter being analyzed in this work. Considering the total attempted exposure time, the overall observing efficiency was approximately 50%.

The last observation of the campaign was executed on 2025 April 1 at 15:32 UTC, and the instrument observed for a total of 1200 s. The orbital track of this operation is shown in Figure 1, along with a visual representation of the HERMES instrument pointing along the orbit and an estimate of the HERMES FOV occulted by Earth. During this observing window, the ADCS system reported that the HERMES instrument was centered within 1° of (R.A., decl.) = ($5^{h}34^{m}$.53, 22.°01) (the Crab coordinates). As a caveat, we note that the accuracy and repeatability of the ADCS has not been independently validated; therefore, a conservative offset of 10° from zenith has been applied to all attitude estimates. However, an offset of this magnitude has a limited impact on these observations, as the sensitivity of the instrument decreases with $\cos\theta$ of the offset angle for a source at zenith.

When correctly configured, the HERMES instrument produces a single data file per second, time-stamped according to the *mock* GPS signal described above. Thus, the 1200 s 2025 April 1 Crab Pulsar/Nebula observation produced 1200 data files. At the time of the observations, onboard file-processing operations were still under commissioning. Consequently, querying the size of all data files required ∼2 hr of computing time, with several attempts needed to overcome the occurrence of PMS resets. Ultimately, a sufficiently complete list of 1023/1200 data files was produced. Figure 3 shows the output of this operation, with the size of each data file plotted against the file time stamp.

Since these data files provide a contiguous list of photon energies and arrival times, the size of each file can be used as a proxy for the total number of photons collected per second, providing a pseudo-lightcurve of the observation. Noticeably, the increased count rates at the beginning and end of the observation ($t < 170$ s, $t > 980$ s) correspond to an expanded electron belt due to the solar flare on 2025 April 1 at ~15:00 UTC, just prior to the observation.

Using this pseudo-lightcurve, any data files exhibiting an excessive count rate (notably while SpIRIT was in the trailing edges of the electron belts, and additionally any temporary

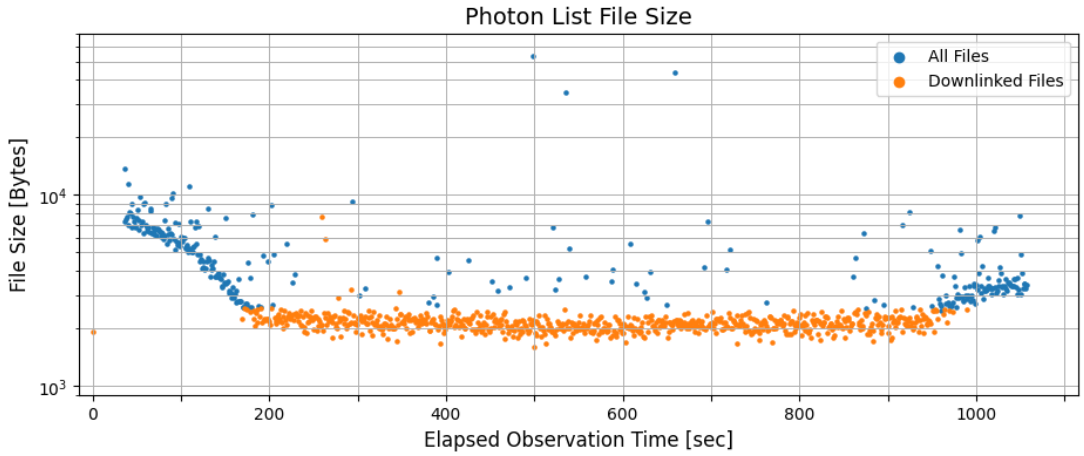

Figure 3. Calibration-mode (CAL) file size vs. elapsed observation time. Only the files in orange were downlinked from the spacecraft, forming the noncontiguous 730 s observation dataset.

spikes) were excluded from the dataset. This threshold was arbitrarily set at 3 kB to manage UHF downlink limitations (with a few exceptions within the first ∼400 s of the observation that were retrieved during earlier downlink attempts as part of a diagnostic process). The included/downlinked files are shown in orange in Figure 3. This process resulted in a list of 730 files, corresponding to 730 noncontiguous seconds of observational data for the Crab Pulsar/Nebula. Given that the files are originated from a single uninterrupted HERMES operation, the internal instrument atomic clock ensures that photon events in the dataset maintain high-precision timing, relative to the nominal submicrosecond precision.

Datasets from observations conducted prior to 2025 April 1 have individual exposure times shorter than 400 s and are therefore insufficient, when considered individually, to yield a statistically significant pulse profile, as discussed below. Moreover, these earlier observations are not considered here because absolute timing is unavailable for combination across HERMES power cycles in the absence of the actual GPS signal for clock synchronization.

3. Crab Absolute Timing

The Crab Pulsar pulse profile is folded into $n_{\rm bins} = 15$ phase channels using the effective SpIRIT exposure of $T_{\rm exp} = 730$ s performed on 2025 April 1 at 15:36:06 UTC described above. Event energies are reconstructed with the standard gain/offset calibration provided by the HERMESDAS reduction pipeline (S. Puccetti et al. 2024). Photons in the 3–22 keV X-mode band are retained. We note that an X-mode detection does not automatically translate into an S-mode detection. For a Crab-like spectrum, the S-mode statistics in the ∼30 keV–2 MeV range are insufficient to yield a significant pulsed profile determination within a single $\lesssim 10^3$ s exposure. While observation stacking would be required, the current SpIRIT/HERMES configuration does not ensure phase connection across segments, preventing a reliable multisegment S-mode detection.

3.1. Barycentric Correction and Ephemeris Folding

Pulse phases were computed by correcting the photon times of arrival with respect to the ephemeris reported in the Jodrell Bank (JB) monthly Crab database,[29] after extrapolating the database solution closest to the observation epoch (2025 March 17, MJD 60751). Other solutions for previous or subsequent epochs were also tested, yielding results similar to those obtained with the original solution.

The spacecraft trajectory was reconstructed by propagating the closest-in-time two-line-element (TLE) orbital ephemeris[30] using the SGP4 algorithm (D. Vallado et al. 2006). Photon arrival times were subsequently converted to the solar system barycenter with the HEASOFT task `barycorr`, adopting the pulsar coordinates in the International Celestial Reference System and the propagated spacecraft ephemeris.

The Crab Pulsar coordinates were taken from the Gaia Data Release 3 (DR3) catalog (Gaia Collaboration et al. 2023).[31] The Gaia DR3 coordinates were propagated from the reference epoch J2016.0 to the observation date by applying the proper motions in R.A. and decl. as

$$\alpha(t) = \alpha_0 + \mu_{\alpha*}\,(t - t_0),$$
$$\delta(t) = \delta_0 + \mu_{\delta}\,(t - t_0), \quad (1)$$

where $\mu_{\alpha*}$ and μ_{δ} are expressed in milliarcseconds per year and reported in the Gaia DR3 catalog.

Starting from the JB solution for the P_0 and $\dot{P}$ quoted in the catalog at $t_0 =$ MJD 60751, we propagate the spin period to the epoch of the SpIRIT observation t:

$$P(t) = P_0 + \dot{P}\,(t - t_0). \quad (2)$$

Hereafter, we adopt the resulting period as the HEASOFT `efold`[32] folding period of the barycentric-corrected time of arrivals.

3.2. Energy-resolved Profile

We select data across several energy bands to assess the impact of noise on signal significance, while keeping the folding parameters constant.

Consistent with the Crab Pulsar spectral energy distribution peaking at 3–5 keV (S. Brandt et al. 2003), we found that the

[29] https://www.jb.man.ac.uk/pulsar/crab/all.gro
[30] See Space-Track TLE archive for SpIRIT on 04-01-2025.
[31] See https://gea.esac.esa.int/archive/, source_id=3403818172572314624.
[32] https://heasarc.gsfc.nasa.gov/docs/software/xronos/examples/efold.html

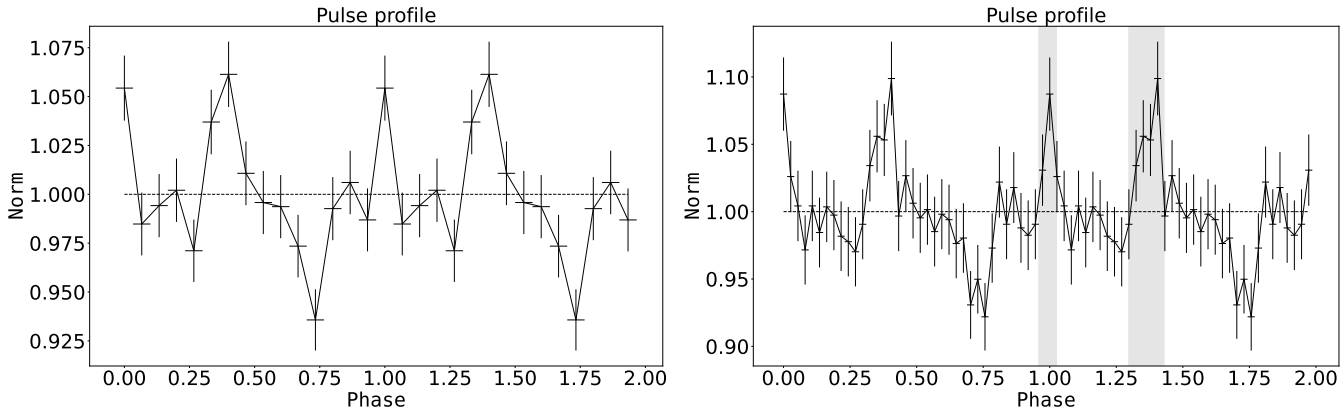

Figure 4. SpIRIT/HERMES Crab pulse profiles in the 3–11.5 keV band; barycentric-corrected times of arrival are folded with $P \simeq 33.84$ ms. Left: 15- channel profile with $\sim 5\sigma$ significance. Right: 37-channel profile with $\sim 4\sigma$ significance. The gray shaded region indicates the peak locations and widths as inferred from the profile in Appendix C.

pulse-profile significance is maximized when a low-energy cut is set to 3 keV. As previously discussed, although the instrument's effective area decreases between 3 and 5 keV and the nominal hardware threshold is ~5 keV, channel-to-channel nonuniform response yields a spread in the *effective* thresholds, allowing nonnegligible acceptance down to ~3 keV.

The profile significance is evaluated by testing the null hypothesis that the data contain a flat signal (i.e., the mean of the profile) and computing the corresponding χ^2:

$$\chi^2 = \sum_{i=1}^{N} \frac{(I_i - \langle I \rangle)^2}{\sigma_i^2}, \tag{3}$$

where I_i is the intensity of the profile and σ_i the associated uncertainties.

The 3–11.5 keV energy range was identified as showing the most significant pulse profile. The obtained profile, folded into 15 phase channels, is shown in Figure 4, with a significance of $\sim 5\sigma$ (i.e., $\chi^2 = 57.5$ with 14 degrees of freedom, dof). This is in agreement with the distribution of expected χ^2 values from the Monte Carlo simulations in Appendix A.2. The pulsation significance evaluated over the full X-mode band (3–20 keV) is $\sim 4\sigma$ (i.e., $\chi^2 = 44$ for dof = 14). This reduced significance at higher energies is driven by the lower Crab Pulsar statistics above 10 keV and by the increasingly background-dominated count rate, with substantial contributions from the cosmic X-ray background and the Crab Nebula emission (D. E. Gruber et al. 1999; M. G. Kirsch et al. 2005).

The phase separation between the two peaks is consistent with the typical Crab profile ($\Delta\phi \approx 0.4$). In particular, the peak widths and phase positions in the 37-bin HERMES profile (Figure 4) agree with those of the schematic RXTE template shown in Appendix C.

Given the uncertainty in the mock GPS time reference, the absolute phase cannot be constrained. Consistently applying several phase shifts to the pulse profile in Figure 4 produces χ^2 values that vary only within the expected statistical scatter (i.e., $\sigma_{\chi^2} = \sqrt{2\,\mathrm{dof}}$). For completeness, the maximum χ^2 occurs for an initial phase offset of six-fifteenths of the period.

These results are nevertheless consistent with an absolute-phase uncertainty arising from time-tagging inaccuracies, themselves a consequence of the absence of onboard GPS time discipline, given that an offset of ± 2.0 s is estimated to be present in the photon time stamps during the observation due to initialization of the HERMES atomic clock with a mock GPS signal based on the main spacecraft computer clock. Injecting systematic shifts in the orbital file within ± 60 s (i.e., corresponding to a positional uncertainty of ± 500 km, far exceeding the expected uncertainty), shows no impact on the pulse-profile shape or significance, apart from a shift in the absolute folding phase. However, we note that while the analysis is robust against absolute time-stamp offsets, these uncertainties do not allow us to determine the absolute pulsar phase for the SpIRIT observation, as reported in the JB catalog.

3.3. Period Blind Search

An independent analysis of the Crab observation was performed using the SKYFIELD and ASTROPY libraries in Python for TLE propagation and barycentric correction. The phase ϕ of each photon was calculated as

$$\phi = \mathrm{mod}\left(\phi_0 + \nu t + \frac{1}{2}\dot{\nu} t^2\right), \tag{4}$$

where the frequency ν and its derivative $\dot{\nu}$ were taken from the JB database as previously discussed. We found the highest two-peak significance at $\phi_0 = 0.4$, consistent with the previous `barycorr`-based analysis to within half a phase-bin width ($1/(2 \times 15) \approx 0.033$). The obtained pulse profile was consistent with the one shown in Figure 4.

From the barycentric-corrected photon arrival times (Skyfield–Astropy correction), we computed in Figure 5 the Lomb–Scargle (LS) periodogram (N. R. Lomb 1976; J. D. Scargle 1982), assigning unit weights to each event. This unbinned approach is computationally efficient and its power normalization is independent of the source flux. We scanned all the periods in the 33–34 ms window, with 1 μs steps. The statistical significance of the LS peaks was estimated via Monte Carlo simulations with 10^5 realizations. Our analysis revealed six formally significant peaks ($>3\sigma$), with the highest ($>3.6\sigma$) matching the Crab period, at $P_{\mathrm{LS}} = 33.9$ ms. A conditioned Monte Carlo test, fixing the Crab peak and randomizing the remaining phases within the Good Time Intervals (GTIs), shows that the other peaks are consistent with GTI-window side lobes, reducing their effective significance to $<1\sigma$. The P_{LS} and its uncertainty were further validated via bootstrap resampling, yielding $\sigma_{\mathrm{LS,bs}} = 30\,\mu$s. With this uncertainty, P_{LS} is consistent with the ephemeris period expected at the epoch of the SpIRIT observation, $P(t)$, within $2\sigma_{\mathrm{LS,bs}}$.

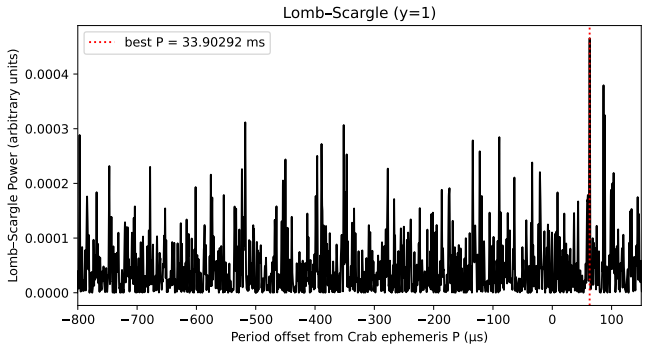

Figure 5. Blind period search with a Lomb–Scargle periodogram in the 33–34 ms range; the highest peak selects the candidate period $P = 33.9$ ms.

4. Instrument Comparison

As a further check of the derived SpIRIT/HERMES pulse profile, we compared it with NICER and NuSTAR data to benchmark the timing performance of SpIRIT and to validate the recovered pulse profile using the NICER/NuSTAR profiles as reference templates. The barycentric correction and folding were applied for the observation epochs as treated in the previous section. Moreover, we used the RXTE Crab pulse profile as a reference template to assess the significance of the pulse profile measured by SpIRIT.

4.1. NuSTAR and NICER Data Extraction

We extract data from the NuSTAR Crab Pulsar observation nearest to the SpIRIT observation, which started on 2025 April 5 at 22:32:21.9340 UTC, with an exposure of $T_{\rm exp} = 14.7$ ks. Data were retrieved from the NuSTAR target search website.[33] We considered filtered data and orbital file as provided by the archive and applied the NuSTAR CALDB clock correction to the event list.

We also retrieved NICER data from the NICER archive.[34] We considered the latest available NICER observation of the Crab Pulsar, taken on 2025 February 28 18:55:18.00, with 1.4 ks exposure time, and downloaded cleaned data with the associated orbital file.

4.2. SpIRIT Profile Modeling

We derive the NuSTAR pulse profile $I_{\rm Nu}$ by considering the same number of channels as the SpIRIT profile in Figure 4. We analyze the SpIRIT profile by fitting it with the model profile:

$$I_{\rm mp} = A \times I_{\rm Nu}(x + \phi) + C, \tag{5}$$

where A is the scale factor of the model and C is an additive constant. The two profiles are not in phase, so we introduce a free parameter ϕ to shift the model in order to minimize the χ^2, which depends on the grade of similarity between the NuSTAR and SpIRIT profiles. $I_{\rm mp}$ is the intensity of the model profile derived from the NuSTAR profile $I_{\rm Nu}$. We fit the SpIRIT profile by minimizing χ^2 with respect to A, C, and the phase shift ϕ, with $\phi \in [0, 1)$. The best-fit phase shift is $\phi = 0.667$, while the best-fit parameters are $A = 0.41 \pm 0.073$ and $C = 0.59 \pm 0.072$.

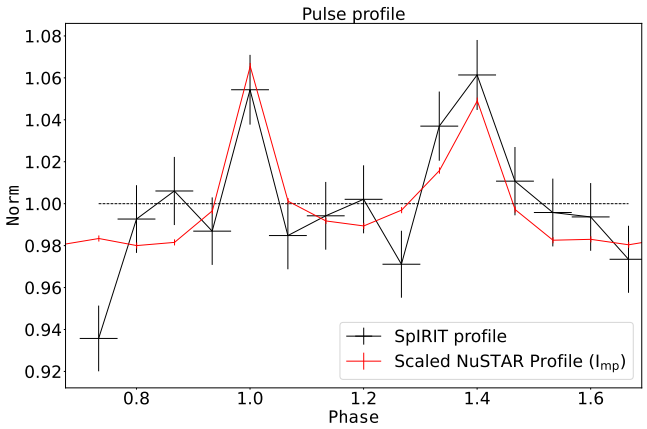

Figure 6. The Crab pulse profile measured by SpIRIT (15 phase bins, 3–11.5 keV) fitted with the NuSTAR model in Equation (5). The solid red curve shows the NuSTAR modulated profile (15 phase bins, 3–11.5 keV) for the best-fit parameters A, C, and ϕ.

Considering the uncertainties associated with the SpIRIT observation and the best-fit parameters (A, C, ϕ), Figure 6 shows the reliability of the pulse profile. The reduced chi-squared is $\chi^2_\nu = 1.33$, with $\nu = 15–2 = 13$ dof (i.e., $\chi^2 = 17.29$). Thus, the data are statistically consistent with the model, and there is no evidence to reject the fit at conventional significance levels.

4.3. Epoch-folding Search

Further proof of the profile accuracy is obtained by performing an epoch-folding search (`efsearch`) around the JB catalog-expected Crab Pulsar ephemeris, as in Equation (2), with a 100 ns resolution. This resolution reflects the accuracy of the onboard time-stamping and therefore limits the precision of the best-period search. The `efsearch` best period is $P_{\rm best} = 33.8394$ ms, which is 0.5 μs smaller than the period derived from the radio ephemeris.

The expected period is highlighted in Figure 7. Its difference from the best `efsearch` period is perfectly compatible with the first-order error on the period determination ΔP, defined as

$$\Delta P = \frac{P^2}{T_{\rm exp}} \approx 1.5\ \mu{\rm s}, \tag{6}$$

where $T_{\rm exp}$ is the observation exposure time, $T_{\rm exp} = 730$ s. However, the Gaussian fit to the narrow `efsearch` peak shows that the SpIRIT best-fit period is consistent with the JB ephemeris at the observation epoch within $\sim 2.5\sigma$, where σ is the standard deviation of the SpIRIT/HERMES Gaussian profile shown in Figure 7.

To compare the timing capabilities of SpIRIT with those of NuSTAR and NICER, we applied `efsearch` to NuSTAR and NICER data in the same energy band used for the `efsearch` in Figure 7. We restricted the exposure so that the resulting detection significance matches that obtained with SpIRIT (see Figure 7) and used the same Crab ephemerides as for the SpIRIT data.

[33] https://heasarc.gsfc.nasa.gov/db-perl/W3Browse/w3table.pl?tablehead=name%3Dnumaster&Action=More+Options
[34] https://heasarc.gsfc.nasa.gov/db-perl/W3Browse/w3table.pl?tablehead=name%3Dnicermastr&Action=More+Options

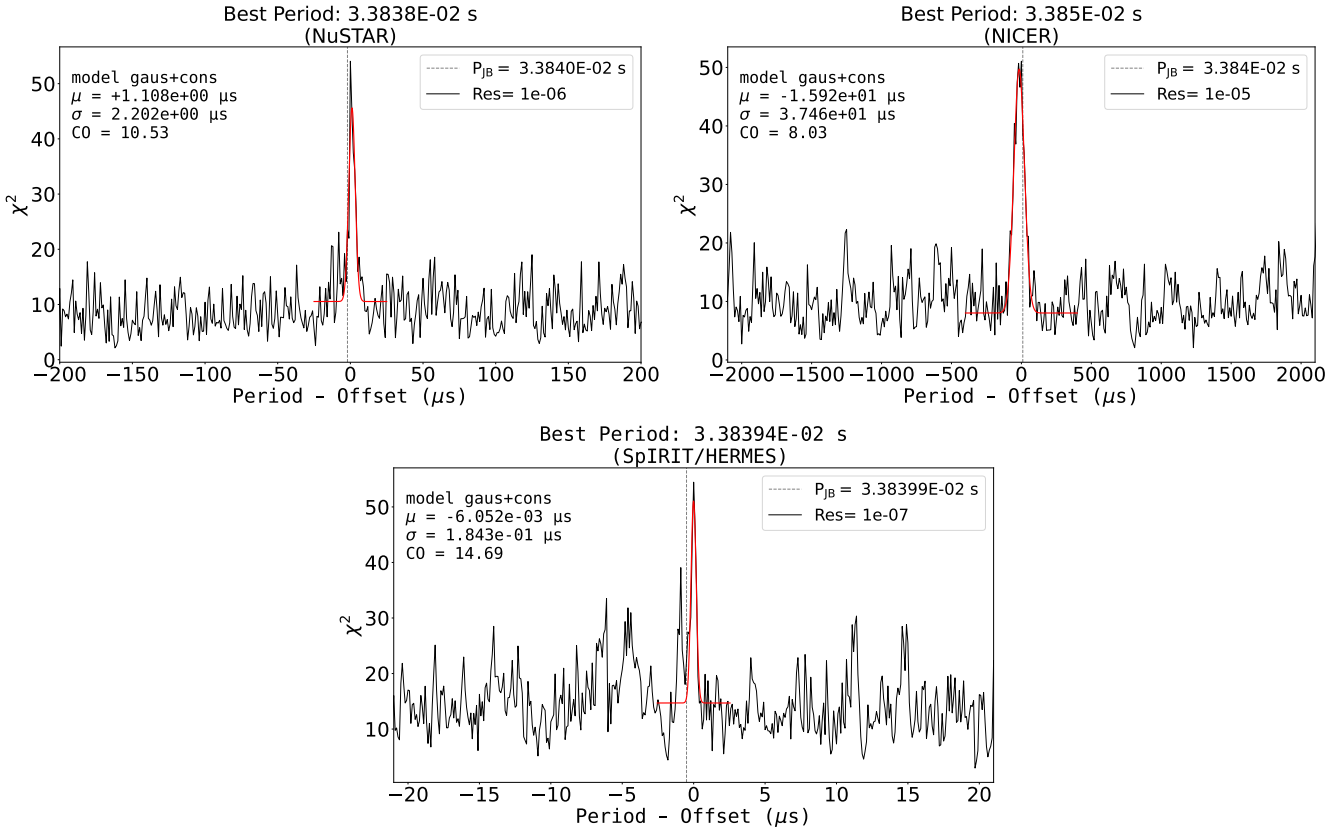

Figure 7. Epoch-folding search around the expected JB catalog period at different search-grid resolutions, depending on the considered exposure time. We used $n_{\rm bins} = 15$ for the 3–11.5 keV energy band and P, $\dot{P}$ relative to the observing epoch. Panels show the Gaussian fit of the `efsearch` for each considered instrument.

Accordingly, the exposure time for NuSTAR and NICER was reduced. The `efsearch` step is then

$$t_{\rm step} = \frac{P^2}{T_{\rm exp}\, n_{\rm bins}}, \tag{7}$$

which sets the period resolution shown in Figure 7. As expected, thanks to the larger effective areas of the two instruments, shorter exposure times are sufficient to reach the HERMES detection significance (≈95 s for NuSTAR and ≈9s for NICER).

4.4. SpIRIT Profile Validation

To validate the correct operation of the SpIRIT/HERMES payload and the observed pulse profile, we compare the measured significance with predictions from the analytical and Monte Carlo analyses in Appendix A.2. We normalize an RXTE Crab Pulsar pulse profile to the count rate (i.e., counts s^{-1}) of the HERMES payload by considering the cosmic X-ray background (CXB) and the Nebula/Pulsar contributions. First, we analytically estimate the exposure time required to achieve a significance of at least $\gtrsim 3\sigma$ (see Appendix B). This analysis confirms that the observed 730 s exposure is sufficient to exceed this threshold.

We then evaluate the statistical power of the detection for the fixed 730 s exposure via Monte Carlo simulations. We generated synthetic realizations of the HERMES pulse profile assuming Poisson statistics, and computed the χ^2 against the mean count rate for each instance. We take as the lower threshold the χ^2 corresponding to a 3σ detection for 15 bins (i.e., $\chi^2_{\rm th,3\sigma} = 35.25$). The results indicate that the probability of obtaining a χ^2 value exceeding this $\chi^2_{\rm th,3\sigma}$ is $P(\chi^2 > \chi^2_{\rm th,3\sigma}) \simeq 82\%$, confirming that the measured significance for the reported Crab profile is fully consistent with the expected noncentral χ^2 distribution (see Appendix A.2).

The consistency between the analytical and Monte Carlo predictions and the observed data validates the instrument performance, indicating that the results are governed by Poisson statistics.

5. Discussion and Conclusion

We performed millisecond X-ray timing using an on-axis dataset of $T_{\rm exp} = 730$ s from a single 1200 s operation, obtained by the wide-FOV HERMES payload on board the 6U ∼11 kg nanosatellite SpIRIT. By folding photon arrival times at the JB ephemeris, extrapolated to the observation epoch, we resolved the canonical Crab Pulsar double-peaked pulse profile with a statistical significance of 5.0σ in the 3–11.5 keV band. The SpIRIT/HERMES pulse shape was validated through a template fit to the closest-in-time NuSTAR observation of the Crab Pulsar.

Moreover, an epoch-folding search of the SpIRIT data recovered a best period of 33.839 ms, only 0.5 μs shorter than the expected catalog value and fully consistent with the Fourier resolution limit of $\Delta P \sim 1.5\,\mu$s achievable with the available SpIRIT/HERMES exposure time.

These results demonstrate that the instrument atomic clock, the SGP4 orbit propagation, and the `barycorr` correction preserve phase coherence to within a few microseconds over the 20 minutes observation window.

To further validate the SpIRIT pulse-profile significance, we carried out an analytical treatment and Monte Carlo simulations using the RXTE Crab pulse profile as a theoretical template. This allowed us to predict the expected significance by taking into account the exposure time and the characteristics of the HERMES payload (e.g., instrument effective area, pointing, response matrix). The computed significance is in full agreement with these predictions, confirming that the instrument is operating correctly and that the measurement process is governed by the expected Poisson statistics.

We conclude that high-precision timing, once restricted to large, resource-intensive observatories, can now be achieved with cost-effective CubeSats. Reaching a $\gtrsim 5\sigma$ detection of a short-period pulsar in just 12 minutes of exposure, using an instrument with a $\lesssim 50\,\mathrm{cm}^2$ instrument effective area, highlights both the effectiveness of the highly compact HERMES payload and the potential of low-cost, rapid-development nanosatellite missions for high-energy astrophysics.

Acknowledgments

This work was supported by the Horizon 2020 program (AHEAD2020, grant Agreement No. 871158; HERMES-SP, grant Agreement No. 821896), and from ASI–INAF agreements for the HERMES Technological Pathfinder (HTP; scientific activities) and HERMES Pathfinder (operations and scientific exploitation). The SpIRIT mission is led by the University of Melbourne (PI: Michele Trenti), which received funding through the International Space Investment – Expand Capability grant funding scheme managed by the ASA for mission development and launch, and through the Moon to Mars – Mission Demonstrator scheme of ASA for mission operations. W.L. acknowledges doctoral funding from the Space Science and Technology PhD program (University of Trento, Cycle XXXVIII). M.D. acknowledges support from the Czech Science Foundation (GACR), project No. 24-11487J.

Appendix A
Crab Pulsar Exposure with HERMES: Analytical Estimate with MC Validation

In general, determining the exposure time required to detect a neutron star pulsed profile is not straightforward. The calculations presented in this appendix show, both analytically and through simulations, how to assess an $n\sigma$-level detection as a function of a given exposure time, $T_{\rm exp}$.

We adopt as a template the folded RXTE (J. H. Swank 1999) pulse profile of the Crab Pulsar reported by C. Jain & B. Paul (2011). Assuming an on-axis pointing, we compute the exposure time required for the two peaks to reach the desired statistical significance.

Using the detector response files, we simulated the count spectrum expected for HERMES with the `fakeit` task in XSPEC, modeling it as the superposition of three components: (i) the Crab Nebula, whose spectral parameters were taken from M. G. Kirsch et al. (2005); (ii) the pulsed emission of the Crab Pulsar, described by the model in M. C. Weisskopf et al. (2011); and (iii) the diffuse X-ray background.

The CXB is derived from the diffuse CXB model proposed in D. E. Gruber et al. (1999). We assume a low-energy HERMES/SpIRIT FOV of 1.57 sr, as in G. Ghirlanda et al. (2024), for the 3–11.5 keV energy band.

In the current configuration of the HERMES instrument on board SpIRIT, the nominal low-energy threshold is set at a level equivalent to about 5 keV. However, the precise energy threshold for each active channel may vary due to channel-to-channel process variations and the discrimination circuit's working principle (Y. Evangelista et al. 2021). This leads to a significant threshold spread, and a particular sensitivity also in the 3–5 keV band. Accordingly, throughout this analysis, we adopted a lower-energy cut of 3 keV.

An appropriate set of HERMES Ancillary Response Files (ARFS) and Redistribution Matrix Files (RMFs) (R. Campana et al. 2021) was generated to take this effect into account. These files were used to evaluate the average count rate in the 3–11.5 keV energy range for the Crab Nebula+Pulsar ($C_{\rm Crab}$) and the CXB ($C_{\rm BKG}$).

A.1. Analytical Determination of the Crab Exposure Time

The dominant practical limitation is the on-axis exposure that can accumulate over time. In this section, we present an analytical treatment for deriving a relation linking the expected χ^2 of the Crab pulse profile to the observing time $T_{\rm exp}$.

Appendix B shows the analytical solution to the problem, and by solving the Equation (B7) for $T_{\rm exp}$, we find that the χ^2 value can be expressed as

$$\chi^2_{\rm th} = T_{\rm exp}\cdot C_{\rm Crab}\cdot \sum_{i=1}^{n_{\rm bins}} \frac{({\rm FRAC}_i - \Delta\phi)^2}{{\rm FRAC}_i + \Delta\phi\cdot\left(\frac{C_{\rm BKG}}{C_{\rm Crab}}\right)}, \qquad \text{(A1)}$$

where FRAC_i is the per-bin pulsed fraction that maximizes the pulse significance, as defined in Appendix C and Equation (C1), and $\Delta\phi$ the dimension of the phase bin.

We now assume as a null hypothesis that the signal is flat in our data (H_0 corresponds to no Crab pulsation detection). The probability that the observed χ^2 exceeds a given threshold $\chi^2_{\rm th,dof}$ comes from the well-known function $\mathrm{P}(\chi^2 \geqslant \chi^2_{\rm th,dof})$, for a certain number of dof.

Equation (A1) can be inverted to derive the $T_{\rm exp}$ necessary to achieve a desired $\chi^2_{\rm th,dof}$ for a given number of bins of $n_{\rm bins}$. We compute the $\chi^2_{\rm th,dof}$ corresponding to a 3σ significance level for each bin, producing the trend shown in Figure 8.

A.2. The Monte Carlo Validation

The previous discussion regards the χ^2 threshold and so the probability $\mathrm{P}(\chi^2 \geqslant \chi^2_{\rm th,dof})$. This establishes the required exposure time to reach a minimum significance limit.

In order to verify the accuracy of the previous solution and the expected χ^2 distribution as a function of a given $T_{\rm exp}$, we perform a simulation-based analysis starting from a theoretical profile with $n_{\rm bins} = 15$, as shown in Figure 10.

We adopt a fixed pulse-shape template and denote its amplitude by I_p (in counts) as the sum of the Crab and background contributions:

$$I_p = I_{\rm ratio}\cdot T_{\rm exp}\cdot C_{\rm Crab} + \frac{1}{n_{\rm bins}}\cdot T_{\rm exp}\cdot C_{\rm BKG}, \qquad \text{(A2)}$$

where $I_{\rm ratio}$ is the ratio of counts in each bin of the RXTE profile over the total counts, as shown in Figure 10. Using Equation (A2), we extract the value of I_p with a Poisson distribution to produce a series of Poisson realizations of the Crab pulse profile at a given exposure time.

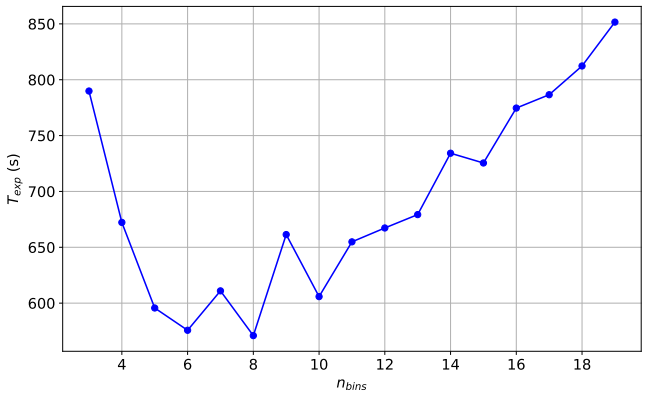

Figure 8. Required exposure time to obtain a χ^2 threshold for a 3σ level detection as a function of $n_{\rm bins}$. Although analytically derived, the observed scatter in Figure 8 arises because the solution is applied to an observed profile with finite counts and is therefore subject to statistical (Poisson) fluctuations.

For each Poisson realization, and according to the exposure time given in Equation (A2), we adopt $T_{\rm exp} = 730$ s and compute the χ^2 relative to the average of the pulse profile.

Appendix B
The Analytical Solution

The Monte Carlo distribution shown in Figure 9 is fitted with a noncentral χ^2 (ncχ^2) distribution:

$$f(x,\ \mathrm{dof},\ \lambda) = \frac{1}{2}\exp\left(-\frac{\lambda + x}{2}\right)\left(\frac{x}{\lambda}\right)^{(\mathrm{dof}-2)/4} \times L_{(\mathrm{dof}-2)/2}(\sqrt{\lambda x}), \quad \text{(B1)}$$

where λ is the noncentrality parameter. $L_{(k-2)/2}$ denotes the modified Bessel function of first order of degree, and x the χ^2. The parameters from the ncχ^2 fit match expectations, and the dof are in line with the theoretical value, $n_{\rm bins} - 1 = 15\text{–}1 = 15$.

Therefore, we expect that in ≈81.58% of cases, a 730 s on-axis HERMES observation will yield at least a 3σ detection.

The total detected count rate (in counts s^{-1}) is given by the sum of the Crab emission (Nebula+Pulsar) $C_{\rm Crab}$ and the background in the HERMES FOV $C_{\rm BKG}$:

$$C_{\rm tot} = C_{\rm Crab} + C_{\rm BKG}. \quad \text{(B2)}$$

If we divide the pulse profile into $n_{\rm bins}$ bins, as in Figure 10, the total rate in each phase bin ϕ_i is

$$C_{\rm tot}(\phi_i) = \Delta\phi \cdot C_{\rm BKG} + \mathrm{FRAC}_i \cdot C_{\rm CRAB} \quad (\mathrm{counts/s}), \quad \text{(B3)}$$

where $\Delta\phi$ is the bin width and FRAC_i the count ratio evaluated for each bin as in Figure 10.

For an observation time $T_{\rm exp}$, the expected counts in each phase bin are

$$N_{\rm tot}(\phi_i) = C_{\rm tot}(\phi_i) \cdot T_{\rm exp}, \quad \text{(B4)}$$

with an associated Poisson error of

$$\sigma_{N_i} = \sqrt{N_{\rm tot}(\phi_i)}. \quad \text{(B5)}$$

The average total value of the expected counts is computed as

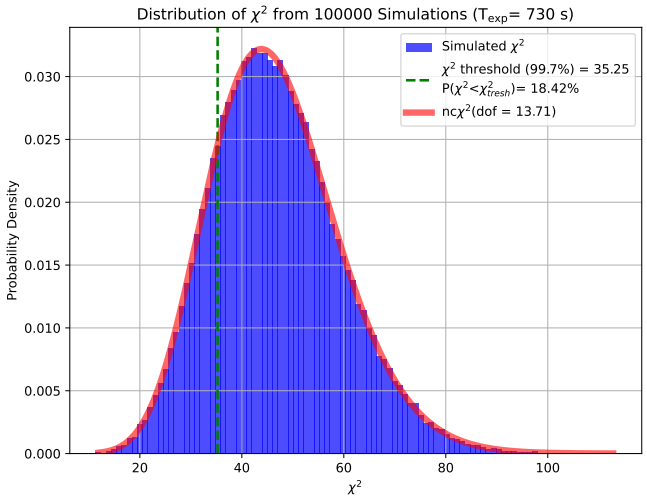

Figure 9. Monte Carlo distribution of the χ^2 statistic for simulated Crab-like pulse profiles with $n_{\rm bins} = 15$. The histogram is fitted with the probability density in Equation (B1). The vertical green line marks the 3σ detection threshold; for dof = 14, we adopt a threshold $\chi^2 = 35.25$, i.e., the 99.7% upper-tail critical value of the central χ^2 distribution.

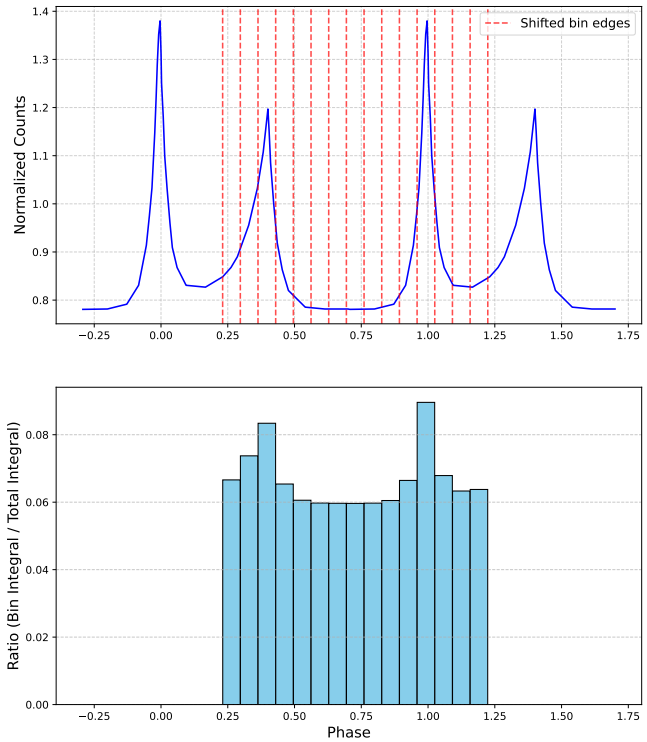

Figure 10. Upper plot: RXTE Crab Pulsar pulse profile rebinned to obtain a 15-channel profile, for the given best shift. Lower plot: normalized count ratio as evaluated in the red bins, with respect to total counts of the profile (FRAC_i). In this case, the on-pulse peaks are the 3rd and the 12th; the others are considered off-pulse bins.

$$\overline{N_{\rm tot}} = \sum_{i=1}^{n_{\rm bins}} \frac{N_{\rm tot}(\phi_i)}{n_{\rm bins}} \times \Delta\phi, \quad \text{(B6)}$$

where $\Delta\phi_{\rm BINS}$ is the peak dimension in unit of phase. We can now compute the theoretical chi-squared value as

$$\chi^2_{\rm th} = \sum_{i=1}^{n_{\rm bins}} \frac{(N_{\rm tot}(\phi_i) - \overline{N_{\rm tot}})^2}{N_{\rm tot}(\phi_i)}. \quad \text{(B7)}$$

Appendix C
Pulsation Significance Maximization

To maximize the pulsation significance, we slide the edges of the phase bins across the folded profile, as shown in Figure 10.

For each trial position, we compute, in every energy channel, the corresponding ratio:

$$\mathrm{FRAC}_i = \frac{N_i}{N_{\mathrm{on}} + N_{\mathrm{off}}}, \quad i = 1,\ldots,n_{\mathrm{bins}}, \tag{C1}$$

i.e., the ratio of counts falling in each bin window N_i to the total counts on-pulse (N_{on}) plus off-pulse (N_{off}), as defined in Figure 10.

The optimal phase shift is found by maximizing the variance:

$$\sigma^2 = \frac{1}{n_{\mathrm{bins}}} \sum_{i=1}^{n_{\mathrm{bins}}} (1 - \mathrm{FRAC}_i)^2, \tag{C2}$$

which reaches its maximum when the binning is such that two bins are centered on the main emission peaks of the pulse profile.

Applying this optimization across different numbers of channels in the 3–11.5 keV energy band, we produce a lookup table recording the phase boundaries and the corresponding FRAC_i for each profile, represented with a given bin number.

ORCID iDs

Wladimiro Leone https://orcid.org/0000-0002-4773-3370
R. Mearns https://orcid.org/0000-0003-1843-6139
T. di Salvo https://orcid.org/0000-0002-3220-6375
L. Burderi https://orcid.org/0000-0001-5458-891X
M. Thomas https://orcid.org/0000-0001-9504-9090
M. Trenti https://orcid.org/0000-0001-9391-305X
F. Fiore https://orcid.org/0000-0002-4031-4157
E. J. Marchesini https://orcid.org/0000-0001-8368-8565
R. Campana https://orcid.org/0000-0002-4794-5453
G. Baroni https://orcid.org/0009-0004-1606-783X
M. Dafčíková https://orcid.org/0009-0000-0365-5940
A. Anitra https://orcid.org/0000-0002-2701-2998
Y. Evangelista https://orcid.org/0000-0001-6096-6710
A. Sanna https://orcid.org/0000-0001-7916-1699
S. Puccetti https://orcid.org/0000-0002-2734-7835
R. Iaria https://orcid.org/0000-0003-2882-0927
S. Barraclough https://orcid.org/0009-0002-0438-2942
M. Ortiz del Castillo https://orcid.org/0000-0001-8431-3765
P. Bellutti https://orcid.org/0000-0001-6732-3654
G. Bertuccio https://orcid.org/0000-0002-7283-021X
A. Chapman https://orcid.org/0000-0002-8946-552X
F. Ceraudo https://orcid.org/0000-0001-9110-3192
T. Chen https://orcid.org/0000-0002-8059-3672
M. Citossi https://orcid.org/0000-0003-3322-234X
R. Crupi https://orcid.org/0009-0005-6714-5161
G. Dilillo https://orcid.org/0000-0002-5132-9821
M. Feroci https://orcid.org/0000-0002-7617-3421
F. Ficorella https://orcid.org/0000-0002-0296-1193
M. Fiorini https://orcid.org/0000-0001-8297-1983
P. Malcovati https://orcid.org/0000-0001-6514-9672
F. Mele https://orcid.org/0000-0002-7882-6879
G. Molera Calvés https://orcid.org/0000-0001-8819-0651
G. Morgante https://orcid.org/0000-0001-9234-7412
D. Novel https://orcid.org/0000-0002-4166-0676
P. Nogara https://orcid.org/0000-0002-4426-3844
A. Nuti https://orcid.org/0000-0002-9352-2355
G. Pepponi https://orcid.org/0000-0002-7397-1946
M. Perri https://orcid.org/0000-0003-3613-4409
A. Picciotto https://orcid.org/0000-0002-4089-9503
R. Piazzolla https://orcid.org/0000-0002-4222-6919
S. Pirrotta https://orcid.org/0000-0003-0377-8937
A. Rachevski https://orcid.org/0000-0002-2723-6297
I. Rashevskaya https://orcid.org/0000-0002-7625-9903
F. Russo https://orcid.org/0000-0002-6216-0240
A. Santangelo https://orcid.org/0000-0003-4187-9560
G. Sottile https://orcid.org/0000-0003-3101-3966
C. Tenzer https://orcid.org/0000-0002-2293-212X
Y. Tao https://orcid.org/0009-0008-2167-078X
A. Vacchi https://orcid.org/0000-0003-3855-5856
G. Zampa https://orcid.org/0000-0003-0238-4469
S. Xiong https://orcid.org/0000-0002-4771-7653
S. Yi https://orcid.org/0000-0001-7599-0174
S. Zhang https://orcid.org/0000-0001-5586-1017
N. Zorzi https://orcid.org/0000-0002-6650-3925

References

Baroni, G., Campana, R., Evangelista, Y., et al. 2024, SPIE, 13093, 130935O
Brandt, S., Budtz-Jørgensen, C., Lund, N., et al. 2003, A&A, 411, L243
Campana, R., Baroni, G., Della Casa, G., et al. 2022, SPIE, 12181, 121815K
Campana, R., Evangelista, Y., Fiore, F., et al. 2024, SPIE, 13093, 130936F
Campana, R., Fuschino, F., Evangelista, Y., Dilillo, G., & Fiore, F. 2021, SPIE, 11444, 114444U
del Castillo, M. O., McRobbie, J., Woods, A., et al. 2025, AcAau, 236, 359
Dilillo, G., Marchesini, E., Della Casa, G., et al. 2024, A&C, 46, 100797
Evangelista, Y., Fiore, F., Campana, R., et al. 2024, SPIE, 13093, 130931Z
Evangelista, Y., Fiore, F., Fuschino, F., et al. 2021, SPIE, 11444, 114441T
Fiore, F., Burderi, L., Lavagna, M., et al. 2021, SPIE, 11444, 114441R
Fiore, F., Trenti, M., Evangelista, Y., et al. 2025, arXiv:2502.17952
Fiore, F., Werner, N., & Behar, E. 2021, Galax, 9, 120
Gaia Collaboration, Vallenari, A., Brown, A. G. A., et al. 2023, A&A, 674, A1
Gandola, M., Mele, F., Grassi, M., Malcovati, P., & Bertuccio, G. 2021, JInst, 16, T12013
Ghirlanda, G., Nava, L., Salafia, O., et al. 2024, A&A, 689, A175
Gruber, D. E., Matteson, J. L., Peterson, L. E., & Jung, G. V. 1999, ApJ, 520, 124
Hurley, K., Pal'shin, V. D., Aptekar, R. L., et al. 2013, ApJS, 207, 39
Jain, C., & Paul, B. 2011, RAA, 11, 1134
Kirsch, M. G., Briel, U. G., Burrows, D., et al. 2005, SPIE, 5898, 22
Leone, W., Burderi, L., Di Salvo, T., et al. 2025, A&A, 701, A50
Lomb, N. R. 1976, Ap&SS, 39, 447
Madsen, K. K., Harrison, F. A., Markwardt, C. B., et al. 2015, ApJS, 220, 8
Mearns, R., Chapman, A., & Trenti, M. 2024, arXiv:2407.19623
Ortiz del Castillo, M., Morgan, J., McRobbie, J., et al. 2024b, arXiv:2404.08399
Ortiz del Castillo, M., Therakam, C., McRobbie, J., et al. 2024a, arXiv:2407.14031
Pál, A., Ohno, M., Mészáros, L., et al. 2023, A&A, 677, A40
Puccetti, S., Perri, M., Campana, R., et al. 2024, SPIE, 13098, 130980O
Rots, A. H., Jahoda, K., & Lyne, A. G. 2004, ApJL, 605, L129
Scargle, J. D. 1982, ApJ, 263, 835
Swank, J. H. 1999, NuPhS, 69, 12
Tamagawa, T., Enoto, T., Kitaguchi, T., et al. 2025, PASJ, 77, 466
Thomas, M., Trenti, M., Sanna, A., et al. 2023, PASA, 40, e008
Trenti, M., del Castillo, M. O., Mearns, R., et al. 2024, arXiv:2407.14034
Vallado, D., Crawford, P., Hujsak, R., & Kelso, T. 2006, in ASC-25: Orbital Dynamics, Perturbations, and Stability/AAS Astrodynamics Specialist Conference and ExhibitAIAA, 2006–6753
van der Klis, M. 2006, in Compact Stellar X-ray Sources, ed. W. H. G. Lewin & M. van der Klis (Cambridge Univ. Press), 39
Vivekanand, M. 2021, A&A, 649, A140
Weisskopf, M. C., Tennant, A. F., Yakovlev, D. G., et al. 2011, ApJ, 743, 139